Mechanical Instability and Interfacial Energy Drive Biofilm Morphogenesis

Jing Yan[a,b,#], Chenyi Fei[b,#], Sheng Mao[a,#], Alexis Moreau[a], Ned S. Wingreen[b], Andrej Košmrlj[a], Howard A. Stone[a,*], Bonnie L. Bassler[b,c,*]

[a]Department of Mechanical and Aerospace Engineering

[b]Department of Molecular Biology

Princeton University, Princeton, NJ 08544 USA

[c]The Howard Hughes Medical Institute, Chevy Chase, MD 20815 USA

#These authors contribute equally.

*Correspondence: bbassler@princeton.edu, hastone@princeton.edu

Summary:

Surface-attached bacterial communities called biofilms display a diversity of morphologies. Although structural and regulatory components required for biofilm formation are known, it is not understood how these essential constituents promote biofilm surface morphology. Here, using *Vibrio cholerae* as our model system, we combine mechanical measurements, theory and simulation, quantitative image analyses, surface energy characterizations, and mutagenesis to show that mechanical instabilities, including wrinkling and delamination, underlie the morphogenesis program of growing biofilms. We also identify interfacial energy as a key driving force for mechanomorphogenesis because it dictates the generation/annihilation of new/existing interfaces. Finally, we discover feedback between mechanomorphogenesis and biofilm expansion, which shapes the overall biofilm contour. The morphogenesis principles we discover in bacterial biofilms, relying on mechanical instabilities and interfacial energies, should be generally applicable to morphogenesis processes in tissues in higher organisms including brain, gut, and lung.

Keywords: Biofilms, mechanobiology, morphogenesis, biomaterial, biointerface, *V. cholerae*, development.

Introduction:

Many of the stunning morphologies that distinguish living entities do not arise exclusively from gene expression programs, but rather from overarching contributions from mechanical forces (Heisenberg and Bellaïche, 2013; Thompson, 1992; Yamada and Cukierman, 2007). Such morphomechanical processes include the formation of ripple-shaped leaves (Liang and Mahadevan, 2009), tendrils and flowers (Gerbode et al., 2012; Liang and Mahadevan, 2011), and the dorsal closure process and apical constriction-mediated epithelial folding during *Drosophila* embryonic development (He et al., 2014; Solon et al., 2009). One key feature is common to many of these morphogenetic transformations: two or more layers of biomaterials are attached to one another but each grows at a different rate (Wang and Zhao, 2015). Inevitably, such growth mismatches generate mechanical stresses, and corresponding shape instabilities, that depend on mechanical and other materials properties of the biological constituents, as well as their geometries. For example, during the development of the human gut, the sequential formation of circular and longitudinal smooth muscle layers restricts the expansion of the underlying softer endoderm and mesenchyme, generating compressive stresses that lead to longitudinal ridges, then a zigzag pattern, and ultimately individual villi (Shyer et al., 2013). Similarly, during late brain development, neurons migrate toward the surface to form the cortical layer, causing tangential expansion of the stiffer cortical gray matter layer relative to the underlying white matter layer, subsequently creating the convoluted surface gyri and sulci (Budday et al., 2014; Tallinen et al., 2016).

Though ancient in their evolutionary origin, bacterial cells can also display intricate developmental patterns, particularly when they exist in the community lifestyle known as biofilms (Ghannoum et al., 2015; Humphries et al., 2017; Persat et al., 2015). Biofilms are surface-associated bacterial communities embedded in a polymer matrix (O'Toole et al., 2000; Thongsomboon et al., 2018) and are a predominant growth mode for bacteria in nature (Hall-Stoodley et al., 2004; Humphries et al., 2017). Biofilms can be beneficial, for example in waste-water treatment (Nerenberg, 2016), but they also cause significant problems in health and industry (Costerton et al., 1999; Drescher et al., 2013) because they are resistant to physical perturbation and antibiotics (Kovach et al., 2017; Meylan et al., 2018). Biofilms on surfaces undergo morphogenic transformations, beginning as smooth colonies and, over time, developing complex morphological features (Beyhan and Yildiz, 2007). Genes specifying matrix components that enable polysaccharide production, cell-surface adhesion, and cell-cell adhesion are required for the morphological transition (Hobley et al., 2015). However, the underlying mechanisms dictating how these biofilm matrix components direct overall morphology are not well-understood. Some models propose spatially distributed differential gene regulation as a driver of biofilm morphogenesis (Okegbe et al., 2014), while other models suggest that localized cell death, together with mechanical forces, give rise to biofilm morphology (Asally et al., 2012). Most recently, theory has been put forward suggesting the possibility of mechanical instabilities being involved in the development of biofilm morphology (Zhang et al., 2017, 2016).

Here, by combining quantitative imaging, biomaterial characterization, mutant analyses, and mechanical theory, we show that the mismatch between the growing biofilm layer and the non-growing substrate causes mechanical instabilities that enable the biofilm to transition from a flat to a wrinkled film, and subsequently to a partially detached film containing delaminated

blisters. The sequential instabilities that the film undergoes, coupled with the generation and annihilation of interfaces, drive the evolution of biofilm topography. Our results demonstrate that bacterial biofilms provide a uniquely tractable system for quantitative investigation of mechanomorphogenesis.

Results:

A mechanical instability model for biofilm morphogenesis

Our central hypothesis is that biofilm morphogenesis is driven by mechanical instabilities that arise from the growth mismatch between an expanding biofilm and the non-growing substrate to which it adheres. To garner evidence for this idea, we grow biofilms on agar plates, which enables us to control the mechanical properties of the substrate by changing the agar concentration (Nayar et al., 2012). We employ a commonly-used *Vibrio cholerae* strain that lacks motility and constitutively produces biofilms (Beyhan and Yildiz, 2007; Yan et al., 2017). This strain (denoted WT) produces biofilms that have disordered cores decorated with radial features extending to the rims (Figure 1A). Indeed, biofilm surface morphology changes with increasing agar concentration: the spacing between the peripheral, radial features is reduced and their amplitudes become more homogeneous.

Encouraged by our above observations and inspired by models developed to describe mechanical instabilities in abiotic materials systems (Li et al., 2012), here we propose a mechanomorphogenesis model for biofilms (Figure 1B). The biofilm originates as a flat film. Its volume increases over time due to cell proliferation and matrix production. If the biofilm were not attached to a substrate, it would grow into a stress-free state to cover a large area (Figure 1B, top, “virtual state”). However, the non-expanding agar substrate constrains biofilm expansion. Thus,

biofilms are always subject to compressive stress (Figure 1B, middle right), which we hypothesize drives the surface morphology. Indeed, a biofilm grown at an air-liquid interface, not limited or compressed by a substrate, exhibits no surface features (Video S1).

According to mechanical instability theories, surface-adhered films under compression have several pathways to release compressive stress (Wang and Zhao, 2015). First, the film can buckle out of the growth plane and deform together with the substrate into a periodically wrinkled pattern (Figure 1B, bottom left). In this mode, the compressive stress is released by film bending and substrate deformation. Alternatively, the film can directly delaminate from the substrate to form "blisters" (Figure 1B, bottom right) (Vella et al., 2009), leaving the substrate essentially undeformed. An extra interfacial energy penalty is paid for delamination since new interfaces are generated, so direct delamination only occurs in systems with weak film-substrate adhesion. Biofilms possesses finite adhesion strength, however (Yan et al., 2018). Thus, we suggest that biofilms first wrinkle, and subsequently delaminate as growth gradually builds up compressive stress. According to this mechanomorphogenesis model, we should be able to change the biofilm topography by changing the spatial distribution of the mechanical stress. To this end, we inoculated two *V. cholerae* biofilms on the same agar plate and allowed them to collide. Indeed, a large localized blister formed at the collision front where mechanical stress is most concentrated (Figure 1C; Video S2).

Our mechanomorphogenesis model provides an intuitive explanation for the commonly observed biofilm surface pattern of a disordered core surrounded by radial features at the edge (DePas et al., 2013; Okegbe et al., 2014; Wilking et al., 2013). Directionality at the edge stems from the asymmetry between the compressive stress on the expanding front that accumulates in the radial and the tangential directions (Figure 1D). During cell proliferation, radial compressive

stress is partially relieved by new biomass extending the biofilm boundary (Zhang et al., 2016). By contrast, in the tangential direction, compressive stress becomes concentrated because there is no analogous relaxation mechanism. Therefore, starting from a flat film, a growing biofilm will undergo mechanical instabilities predominantly in the tangential direction, leading to radial wrinkling, and later, delamination patterns (Figure 1D). In contrast, in the interior region of a biofilm, compressive stress occurs in both the radial and tangential directions, giving rise to a network containing both radially- and tangentially-oriented features (Figures 1A and 1D). To demonstrate that pattern directionality is determined by expansion anisotropy, we changed the biofilm growth geometry by inoculating cells starting from a line so the biofilm would extend quasi-unidirectionally (Video S2). In this geometry, compressive stress along the inoculation line is higher than that perpendicular to the line (the expanding direction). Therefore, wrinkles/blisters occur perpendicular to the biofilm line (Figure 1E).

A trilayer mechanical model predicts the biofilm wrinkling wavelength

Mechanical instability theory predicts that, for a film-substrate system that is subject to compressive stress, the wrinkling wavelength is determined exclusively by the thickness and mechanical properties of the relevant materials (Huang et al., 2005). If so, we would expect the wrinkle wavelength to change with the mechanical properties of the biofilm and substrate but be independent of the growth stage and geometry of the biofilm. To extract the wrinkle wavelength, we imaged the biofilm morphogenesis process over 72 h and quantified the periodicity of radial stripes (Figure S1; Videos S3-5). We note that blisters emerge from wrinkles and they inherit the wavelength of wrinkles, so we do not distinguish between the two in this analysis. We quantified the number of wrinkles/blisters N as a function of radial distance r from the biofilm center at

different times. We found a linear relationship between N and r (Figures 2A and S1). The slope has a geometrical origin: $N = (2\pi/\lambda)r$ in which λ is the inherent wavelength of the system irrespective of the time in the developmental process or the location in the overall pattern. A constant wavelength λ also means that radial wrinkles/blisters must bifurcate to maintain constant spacing as r increases, and indeed, we observed this to be the case (Figure 2A, inset). We also confirmed that the same λ is maintained when cells were inoculated in the line geometry and grew quasi-unidirectionally (Figure S1). We conclude that the wavelength of wrinkles/blisters reflects an intrinsic physical property of the biomechanical system.

Mechanical instability theory also predicts how wavelength varies with the stiffness contrast between the biofilm and the substrate. Classical linear instability theories for bilayer film-substrate systems predict that λ, normalized by the film thickness h, should be equal to $2\pi(G_f/G_s)^{1/3}$, in which G_f and G_s are the shear modulus of the film and the substrate, respectively (Chen and Hutchinson, 2004; Huang et al., 2005). The 1/3 power law is a result of the competition between the energy cost to deform the film and that to deform the substrate. To test whether this relationship applies to biofilms, we measured λ, h, G_s, and G_f for all growth conditions. G_f varies minimally over a wide range of agar concentrations, while G_s varies by almost three orders of magnitude for agar concentrations from 0.4% to 3% (Table S1). Plotting λ/h versus G_f/G_s on a log-log scale (Figure 2B) reveals the characteristic scaling power law of 1/3, indicating the applicability of mechanical instability theory to biofilm morphogenesis.

One key discrepancy exists between the experimental measurements and the bilayer model. Theory predicts that, if $G_f/G_s < 1.3$, the substrate is too stiff for the flat-to-wrinkling transition to occur (Wang and Zhao, 2015). However, wrinkling occurs in our experiments for G_f/G_s well below 1.3 corresponding to agar concentrations $\geq 0.7\%$. To reconcile this discrepancy, we considered

that a third soft, intermediate layer could exist between the growing biofilm and the non-growing substrate, which has been shown to allow wrinkling behavior even at low G_f/G_s ratio (Lejeune et al., 2016a).

To acquire evidence for an intermediate layer, we employed a capillary peeling method in which biofilms are gently dipped into water and capillary force peels the biofilm off the substrate without destroying the biofilm or the underlying surface (Figure S2) (Yan et al., 2018). Indeed, an ~ 10 μm residual layer remains on the substrate after peeling (Figure 2C). Staining shows it consists primarily of matrix polysaccharide debris (Figure S2). We measured the thickness of the debris layer h_d for each growth condition, and replotted our data using the corrected biofilm thickness h_f, obtained by subtracting h_d from the total biofilm thickness h (Figures 2D and S2). To rationalize the replotted curve, we took advantage of recent modeling efforts concerning multi-layer wrinkling phenomena (Lejeune et al., 2016a). The only unknown parameter in our work is the shear modulus of the debris layer, G_d. In our simulation, we use a debris layer thickness $h_d = 0.3h_f$, obtained from our experimental measurements and we left G_d/G_f as a fitting parameter (Figure S3). The trilayer model qualitatively and quantitatively captures our experimental observations. Qualitatively, with a soft intermediate layer, the wrinkling pattern persists even when the substrate becomes stiffer than the biofilm ($G_s > G_f$). Unlike the bilayer model in which the substrate is deformed by the wrinkling film, in the trilayer model, the soft interfacial layer assumes the major share of the deformation, effectively reducing the substrate stiffness (Figures 2D and S3) (Lejeune et al., 2016a). Quantitatively, predictions from the trilayer model recapitulate the prominent features of the revised plot: λ/h_f scales according to the bilayer model as $2\pi(G_f/G_s)^{1/3}$ for large G_f/G_s ratios, but increasingly deviates from the 1/3 scaling law for smaller G_f/G_s values. In the low G_f/G_s regime, wrinkling is increasingly controlled by the soft intermediate layer. An

intermediate layer stiffness of $G_d = 0.1G_f$ allows the trilayer model to best fit our experimental data over all conditions.

The biofilm wrinkling-to-delamination transition is controlled by interfacial energy and substrate stiffness

We next investigated the second transition predicted by our mechanomorphogenesis model: wrinkling-to-delamination. Whether and when a film-substrate system undergoes delamination is controlled by a competition between the adhesion energy between layers, Γ , and the elastic energy in the substrate (Wang and Zhao, 2015). A dimensionless term Γ^*, defined as Γ/hG_s, was used previously to quantify the relative importance of the two energies (Wang and Zhao, 2015). We recently measured the biofilm-agar interfacial adhesion energy Γ~5-10 mJ/m^2 (Yan et al., 2018). Hence, Γ^* is on the order of 0.01~1 in the current system, making delamination highly likely to occur during biofilm growth. In the context of the trilayer model, delamination takes place at the weakest interface, which is between the biofilm and the debris layer.

To experimentally access the wrinkling-to-delamination transition, we simultaneously imaged the growing biofilm from the top and the side (Figures 3A and S1). Radial wrinkles developed into blisters when growth proceeded beyond ~36 h. At low agar concentrations, large amplitude blisters emerged among small amplitude wrinkles (Figure 3A). At higher agar concentrations, additional wrinkles developed into blisters, although with amplitudes smaller than those on low concentration agar substrates. We verified these findings using optical profiling to capture the full three-dimensional (3D) height information of the entire biofilm (Figure 3B). To peer inside blisters, we imaged cross-sectioned biofilms grown from cells producing fluorescence from *mKate2* (Figure 3C). At low agar concentration (i.e., 0.6%), only a small fraction of wrinkles

were detached from the substrate in the form of blisters (Figure S4). In contrast, at high agar concentration (i.e. 1.0%), nearly all wrinkles had developed into blisters. In the cross-sectional images, voids were clearly present underneath the blisters, presumably filled with liquid (Wilking et al., 2013). Figure 3D quantifies the positive correlation between the percentage of wrinkles that converted to blisters at the biofilm edge and the substrate agar concentration.

To rationalize the dependence of the delamination pattern on agar concentration, it is useful to recall the notion of normalized adhesion energy, Γ^*. On stiff substrates, Γ^* is small so delamination is favored over wrinkling. Blisters form extensively but they are small because they share the overall compressive stress. On soft substrates, Γ^* is large so blisters form only infrequently while the majority of the biofilm remains attached to the substrate. In this case, the isolated blisters concentrate the compressive stress and become larger than those on a stiff substrate. These large blisters also suppress nearby wrinkles from delaminating, presumably because the biofilm and the substrate can slide relative to one another such that a blister drags nearby biofilm material towards it, and in so doing, releases compressive stress in the vicinity. We hypothesized that the locations of blisters on soft substrates are defined by surface defects that trigger local delamination. To test this possibility, we made surface imperfections in the soft agar substrate at defined positions (Figure 3E). Indeed, these imperfections dictated the exact locations at which blisters formed as the biofilm expanded. By contrast, on stiff substrates, delamination occurred along the entire biofilm rim irrespective of the predefined surface imperfections (Figure 3E).

Interfacial energy controls blister development dynamics and interactions between blisters

In conventional materials systems, a blister assumes a sinusoidal profile and continues to develop in both width and height as compressive stress increases (Vella et al., 2009). We wondered whether the dynamics of blisters in a living, growing biofilm would follow the same principles. We tracked isolated blisters by imaging the expanding biofilm rim (Figure S1). Surprisingly, the width of each blister decreased while its height increased over time (Figure 4A). The traces of the height profile show that, over time, the two sides of a biofilm blister approach and then attach to each other, and subsequently, the blister continues to develop only in the height direction (Figure 4B). Consistent with this finding, the blister width levels off at a value of twice the biofilm thickness. We also analyzed interactions between blisters at late stages of biofilm development (> 48 h). Neighboring blisters tend to merge into single dark features in the transmission images (Figure 4C, top), causing the total number of blisters N to decrease at the biofilm rim over long times (Figure S4). Cross-sectional images reveal that head-to-head contact occurred (Figure 4C, bottom).

The biofilm blister dynamics described above involve generation/annihilation of new/existing interfaces, which have energy penalties/payoffs. To understand the order of these events, we measured their interfacial energies in WT *V. cholerae* biofilms. They are: biofilm blister-liquid under it, $\gamma_{fl} \sim 49$ mJ/m^2; biofilm blister-air above it, $\gamma_{fa} \sim 30$ mJ/m^2; and the energy needed to separate the biofilm from the debris layer under it, $\Gamma \sim 5$ mJ/m^2 (Figure 4D). This energy hierarchy determines the sequence through which interfaces are generated/annihilated (Figure 4E). First, compressive stress leads to delamination of the biofilm from the debris layer, forming a local blister. This step generates an additional high-energy interface between the blister and the liquid underneath it. To eliminate this high-energy interface, the two sides of the inner face of the blister adhere to each other as the blister grows. Once this self-adhering configuration arises, the blister

can only develop in the vertical direction. However, blister growth enlarges the interface between the biofilm and the air. Subsequent merging of neighboring blisters (Figure 4C) eliminates biofilm-air interfaces, and, in so doing, lowers the free energy of the entire system.

If the above interpretations are correct, changing the relative magnitudes of the three interfacial energies should modulate blister dynamics, and, in turn, the global biofilm morphogenesis process. To test this idea, we deleted *bap1* and *rbmC* encoding proteins responsible for cell-surface interactions and biofilm hydrophobicity (Fong and Yildiz, 2007; Berk et al., 2012; Hollenbeck et al., 2014). Rather than forming isolated blisters, the Δ*bap1*Δ*rbmC* biofilm exhibits a star-shaped morphology with flat regions between the facets of the stars (Figure 5A, top) (Yan et al., 2017). The cross-section of a single facet shows that it consists of a group of congregated blisters (Figure 5A, bottom). Curiously, in contrast to the WT blisters, in the mutant, only the external surfaces of neighboring blisters adhere, leaving the internal spaces under each blister intact. Indeed, transmission images show that multiple stripes exist within one facet, corresponding to multiple blisters (Figures 5B and S4).

To rationalize the Δ*bap1*Δ*rbmC* blister dynamics, we measured the relevant interfacial energies (Figure 5C). The adhesion energy Γ between the Δ*bap1*Δ*rbmC* biofilm and the substrate is below the detection limit, meaning that delamination occurs more easily in the Δ*bap1*Δ*rbmC* biofilm than in the WT biofilm. Indeed, Δ*bap1*Δ*rbmC* biofilm blisters emerge directly from the expanding flat film, skipping the wrinkling state (Video S6). Second, the relative order of interfacial energies changes in the mutant: γ_{fl} approaches zero while γ_{fa} is large, consistent with the hydrophilicity of the Δ*bap1*Δ*rbmC* biofilm (Hollenbeck et al., 2014). These alterations in interfacial energies have profound consequences on blister dynamics (Figure 5D). Instead of annihilating biofilm-liquid interfaces inside of blisters, in the mutant, neighboring blisters prefer

to collapse against each other, which eliminates the high energy interface between the biofilm and the air. Indeed, during the development of the mutant biofilm, newly-emergent blisters move towards, and ultimately join existing blister groups (Figure 5E; Video S6). The triangular shape of each facet in the Δ*bap1*Δ*rbmC* biofilm is therefore a consequence of the merging of multiple blisters, whose ages and radial lengths decrease from the center to the edge of the aggregate.

Mechanical instability and colony expansion feed back onto one another

We wondered whether the emergence of the 3D biofilm surface topography affected biofilm expansion in the growing plane. One common morphological feature of bacterial biofilms is the irregular petal-shaped 2D contours (Videos S3 and S4). We hypothesized that the evolution of contours could also be a consequence of mechanical instability. To quantify the contour undulation, we define the asphericity parameter $\alpha = P^2/4\pi A$, in which P is the perimeter of the biofilm and A is the area (Asally et al., 2012). $\alpha = 1$ for a perfect circle. For a biofilm growing on soft agar (0.4%, Figure 6A), there is a sharp increase in α at t_c, the time at which the 3D surface morphology forms at the edge (Figure S5). To show that blisters are required for contour undulations, we tracked α for mutant biofilms lacking the matrix structural polysaccharide (Δ*vpsL*) (Hammer and Bassler, 2003) or lacking matrix structural proteins (Δ*rbmA*Δ*bap1*Δ*rbmC*) (Berk et al., 2012; Yan et al., 2017). In both cases, the biofilm has no surface features and α remains close to 1 (Figure 6A).

To investigate the coupling between contour undulations and biofilm morphogenesis in the z direction, we followed the time evolution of a growing biofilm border (Figure 6B). Visually, the indentations along the contours always correspond to the locations of large blisters. To quantify this finding, we measured the local curvature κ and expansion velocity V_f along the biofilm

periphery (Figures 6B, 6C and S5). Both κ and V_f are negatively correlated with the positions of blisters. Monitoring the evolution of a single blister and a nearby flat region shows a transient large difference in V_f when the blister initially forms at the edge (~ 45 h in this case; Figure 6D), which triggers the local contour indentation. The emergence of a blister creates an extra dimension into which newly produced biomass can be distributed, which causes local slowing in V_f, thus establishing the correlation between blister locations and negative local curvature. After this transient difference, V_f becomes comparable for boundaries with and without blisters, and the local curvature reaches a steady value, provided that there is no nearby blister (Figure S4). In this steady state, the pedal-like contour propagates radially without changing the overall shape of the contour. This explanation for the formation of the biofilm petal shapes suggests that contour undulations require non-homogeneous blister distribution along the biofilm rim and indeed, WT biofilms grown on stiff agar (> 1.0%) remain nearly circular because they possess regularly and closely spaced blisters (Figure 6A, blue line). Thus, the 3D surface topography that arises due to mechanical instabilities caused by biofilm expansion, in turn, feeds back to regulate biofilm expansion and contour evolution.

Discussion

We show here that mechanical instabilities, including wrinkling and delamination, underlie biofilm morphogenesis. Moreover, differences in interfacial energies drive mechanomorphogenesis by dictating the creation/annihilation of new/existing interfaces. Finally, feedback between mechanomorphogenesis and biofilm expansion shapes the overall biofilm contour. Such a quantitative understanding of biofilm morphology should facilitate discovery of

new genes and/or new compounds that encode/modulate biocomponents that specify global biofilm morphology.

Morphological patterns can certainly involve gene regulation programs. Nonetheless, we expect our mechanical instability findings in *V. cholerae* biofilms to apply to other systems – from bacteria to human – because they reveal links between the specific materials properties of the biological components and morphological transitions. Regarding bacterial systems, take for example, *Pseudomonas aeruginosa*, an opportunistic pathogen (Costerton et al., 1999). Mutants that are incapable of phenazine production (Δ*phz*) form biofilm topographies similar to those we examine here - disordered cores surrounded by radial features (Dietrich et al., 2013). In contrast, WT *P. aeruginosa* develops biofilms with labyrinthine pattern surrounded by flat rims. We suggest that the same mechanical principles uncovered here drive the morphological transitions in *P. aeruginosa*. The Δ*phz* mutant, which overproduces extracellular polysaccharides (Madsen et al., 2015), behaves in exactly the same manner as we described here. WT *P. aeruginosa* cells, on the other hand, form a structured biofilm only in the interior of the colony but not at the rim in the early stages of biofilm development (Madsen et al., 2015). In this case, cells at the colony center display upregulated matrix production, but their expansion is constrained by cells located at the periphery that are downregulated for matrix production (Madsen et al., 2015); the resulting radial compression gives rise to labyrinthine wrinkles/blisters. As another example, in *Bacillus subtilis* biofilms, nutrient limitation causes significant cell death at the biofilm core (Asally et al., 2012), providing local outlets for the accumulated compressive stress. In the framework of our model, localized cells death can be viewed as the source of surface defects that function to trigger local delaminations. The characteristic length scale generated via the cell death mechanism, however, differs from that predicted by our current work (Figure S2). These examples illustrate how gene

regulation and spatially-distinct cell physiology can be coupled to mechanical instability to promote spectacular biofilm surface morphologies.

Recent theoretical work on bacterial biofilms has considered mechanical instabilities. Zhang *et al.* used simulations to suggest that anisotropic growth coupled with wrinkling instability could generate the surface topographies observed in bacterial biofilms (Zhang et al., 2016), and most recently they considered the possibility of delamination (Zhang et al., 2017). Wang *et al.* introduced competition between adhesive and elastic energy, and computed a phase diagram of the different modes of instability for a film-substrate system (Wang and Zhao, 2015). These inspiring theories will become more valuable by inclusion of the measured biophysical parameters and additional observations generated through experiments. For example, the thin intermediate debris layer we discovered here is not accurately considered in biofilm simulations, but is required to explain the wrinkling instability in biofilms (Figure 2D). Additionally, interfacial energies play a predominant role in driving morphologies of biological materials that possess soft layers, whereas their roles are minor in classical mechanical systems (Qi et al., 2011). To date, the contributions from interfacial energies have not been considered in mechanical theories developed for biological systems. Future theoretical analyses can now incorporate measured parameters to understand the rich hierarchical dynamics and the history dependence of mechanomorphogenesis, taking into account biofilm viscoelasticity, interfacial energies, and the consequences of sliding and friction between the biofilm and the substrate (Beroz et al., 2018; Peterson et al., 2015).

Though more sophisticated, eukaryotic organisms often employ similar mechanical instability principles to generate fascinating morphologies. Thus, our findings for biofilms are potentially generalizable and relevant for studies of development in higher organisms. In addition to the development of brain and gut mentioned in the introduction, a configuration of multiple

layers with different stiffnesses and growth rates is also employed during lung morphogenesis to precisely control the spatial placement of epithelial bifurcations, ultimately defining the global architecture of the lung (Kim et al., 2015). An even closer analogy is presented by cerebellum development. The cerebellum possesses a thin, soft layer of Purkinje cells that is sandwiched between the rapidly-growing external granular layer and the slow-growing internal granular layer (Lejeune et al., 2016b). Through wrinkling instabilities, the cerebellum develops finely spaced parallel grooves called folia. This hard-soft-hard geometry and the associated wrinkling instabilities directly mirror the configuration we discovered in *V. cholerae* biofilms. Hence, our work suggests that exploiting mechanical principles to drive key morphogenic events is ancient: it occurs in bacteria, and evolution, as is often the case, has reused prokaryotic processes and principles in eukaryotes. Notably, however, to our knowledge, analogous examples of the overarching role of interfacial energies in driving morphogenesis have not been reported for eukaryotic systems. Thus, exploiting interfacial energy differences to dictate morphology could be a unique feature of bacterial communities. In summary, biofilms represent an intriguing and highly tractable model system to investigate the general role of mechanical forces in morphogenesis and they provide a convenient system for morpho-engineering.

Acknowledgements

This work was supported by the Howard Hughes Medical Institute (B.L.B.), National Science Foundation Grants MCB-1713731 (B.L.B) and MCB-1344191 (to N.S.W., B.L.B., and H.A.S.), NIH Grant 2R37GM065859 (B.L.B.), and the Max Planck Society-Alexander von Humboldt Foundation (B.L.B.). J.Y. holds a Career Award at the Scientific Interface from the Burroughs

Wellcome Fund. We thank Ms. Quiting Zhang and Dr. Jie Yin for helpful discussions and Dr. Paul Shao, Dr. Yao-Wen Yeh, Prof. Craig Arnold, and Keyence for instrument support.

Author Contributions:

J.Y., S.M., H.A.S., and B.L.B. initiated this work. J.Y., C.F., and A.M. performed the experiments. J.Y., C.F., S.M., H.A.S., and B.L.B. analyzed the data. S.M., C.F., and A.K. performed the simulations and theoretical analysis. All authors contributed to writing the paper.

Competing financial interests

The authors declare no competing financial interests.

References

Ahrens J, Geveci B, Law C. 2005. ParaView: An end-user tool for large data visualizationThe Visualization Handbook. Cambridge: Academic Press. pp. 717–731. ISBN:978-0-12-387582-2

Alnæs M, Blechta J, Hake J, Johansson A, Kehlet B, Logg A, Richardson C, Ring J, Rognes ME, Wells GN. 2015. The FEniCS Project Version 1.5. *Arch Numer Software* **3**:9–23. doi:10.11588/ans.2015.100.20553

Asally M, Kittisopikul M, Rué P, Du Y, Hu Z, Çağatay T, Robinson AB, Lu H, Garcia-Ojalvo J, Süel GM. 2012. Localized cell death focuses mechanical forces during 3D patterning in a biofilm. *Proc Natl Acad Sci USA* **109**:18891–18896. doi:10.1073/pnas.1212429109

Berk V, Fong JCN, Dempsey GT, Develioglu ON, Zhuang XW, Liphardt J, Yildiz FH, Chu S. 2012. Molecular architecture and assembly principles of *Vibrio cholerae* biofilms. *Science* **337**:236–239. doi:10.1126/science.1222981

Beroz F, Yan J, Meir Y, Sabass B, Stone HA, Bassler BL, Wingreen NS. 2018. Verticalization of bacterial biofilms. *Nat Phys* **14**:954–960. doi:10.1038/s41567-018-0170-4

Beyhan S, Yildiz FH. 2007. Smooth to rugose phase variation in *Vibrio cholerae* can be mediated by a single nucleotide change that targets c-di-GMP signalling pathway. *Mol Microbiol* **63**:995–1007. doi:10.1111/j.1365-2958.2006.05568.x

Budday S, Raybaud C, Kuhl E. 2014. A mechanical model predicts morphological abnormalities in the developing human brain. *Sci Rep* **4**:5644. doi:10.1038/srep05644

Chen X, Hutchinson JW. 2004. Herringbone buckling patterns of compressed thin films on compliant substrates. *J Appl Mech* **71**:597–603. doi:10.1115/1.1756141

Costerton JW, Stewart PS, Greenberg EP. 1999. Bacterial biofilms: a common cause of persistent infections. *Science* **284**:1318–1322. doi:10.1126/science.284.5418.1318

DePas WH, Hufnagel DA, Lee JS, Blanco LP, Bernstein HC, Fisher ST, James GA, Stewart PS, Chapman MR. 2013. Iron induces bimodal population development by *Escherichia coli*. *Proc Natl Acad Sci USA* **110**:2629–2634. doi:10.1073/pnas.1218703110

Dietrich LEP, Okegbe C, Price-Whelan A, Sakhtah H, Hunter RC, Newman DK. 2013. Bacterial community morphogenesis is intimately linked to the intracellular redox state. *J Bacteriol* **195**:1371–1380. doi:10.1128/JB.02273-12

Drescher K, Shen Y, Bassler BL, Stone HA. 2013. Biofilm streamers cause catastrophic disruption of flow with consequences for environmental and medical systems. *Proc Natl Acad Sci USA* **110**:4345–4350. doi:10.1073/pnas.1300321110

Fong JCN, Yildiz FH. 2007. The rbmBCDEF gene cluster modulates development of rugose colony morphology and biofilm formation in *Vibrio cholerae*. *J Bacteriol* **189**:2319–2330. doi:10.1128/JB.01569-06

Gerbode SJ, Puzey JR, McCormick AG, Mahadevan L. 2012. How the cucumber tendril coils and overwinds. *Science* **337**:1087–1091. doi:10.1126/science.1223304

Geuzaine C, Remacle J-F. 2009. Gmsh: A 3-D finite element mesh generator with built-in pre- and post-processing facilities. *Int J Numer Method Eng* **79**:1309–1331. doi:10.1002/nme.2579

Ghannoum M, Parsek M, Whiteley M, Mukherjee P. 2015. Microbial Biofilms, 2nd ed. Washington, DC: ASM Press. ISBN:978-1-55581-745-9

Hall-Stoodley L, Costerton JW, Stoodley P. 2004. Bacterial biofilms: from the natural environment to infectious diseases. *Nat Rev Microbiol* **2**:95–108. doi:10.1038/nrmicro821

Hammer BK, Bassler BL. 2003. Quorum sensing controls biofilm formation in *Vibrio cholerae*. *Mol Microbiol* **50**:101–104. doi:10.1046/j.1365-2958.2003.03688.x

He B, Doubrovinski K, Polyakov O, Wieschaus E. 2014. Apical constriction drives tissue-scale hydrodynamic flow to mediate cell elongation. *Nature* **508**:392–396. doi:10.1038/nature13070

Heisenberg C-P, Bellaïche Y. 2013. Forces in tissue morphogenesis and patterning. *Cell* **153**:948–962. doi:10.1016/j.cell.2013.05.008

Hobley L, Harkins C, Macphee CE, Stanley-Wall NR. 2015. Giving structure to the biofilm matrix: an overview of individual strategies and emerging common themes. *FEMS Microbiol Rev* **39**:649–669. doi:10.1093/femsre/fuv015

Hollenbeck EC, Fong JCN, Lim JY, Yildiz FH, Fuller GG, Cegelski L. 2014. Molecular determinants of mechanical properties of *V. cholerae* biofilms at the air-liquid interface. *Biophys J* **107**:2245–2252. doi:10.1016/j.bpj.2014.10.015

Huang ZY, Hong W, Suo Z. 2005. Nonlinear analyses of wrinkles in a film bonded to a compliant substrate. *J Mech Phys Solids* **53**:2101–2118. doi:10.1016/j.jmps.2005.03.007

Humphries J, Xiong L, Liu J, Prindle A, Yuan F, Arjes HA, Tsimring L, Süel GM. 2017. Species-independent attraction to biofilms through electrical signaling. *Cell* **168**:200–209. doi:10.1016/j.cell.2016.12.014

Jones RM. 2009. Deformation Theory of Plasticity. Blacksburg: Bull Ridge Publishing. ISBN:978-0-9787223-1-9

Kim HY, Pang M-F, Varner VD, Kojima L, Miller E, Radisky DC, Nelson CM. 2015. Localized smooth muscle differentiation is essential for epithelial bifurcation during branching morphogenesis of the mammalian lung. *Dev Cell* **34**:719–726. doi:10.1016/j.devcel.2015.08.012

Kovach K, Davis-Fields M, Irie Y, Jain K, Doorwar S, Vuong K, Dhamani N, Mohanty K, Touhami A, Gordon VD. 2017. Evolutionary adaptations of biofilms infecting cystic fibrosis

lungs promote mechanical toughness by adjusting polysaccharide production. *npj Biofilms Microbiomes* **3**:1. doi:10.1038/s41522-016-0007-9

Lejeune E, Javili A, Linder C. 2016a. Understanding geometric instabilities in thin films via a multi-layer model. *Soft Matter* **12**:806–816. doi:10.1039/C5SM02082D

Lejeune E, Javili A, Weickenmeier J, Kuhl E, Linder C. 2016b. Tri-layer wrinkling as a mechanism for anchoring center initiation in the developing cerebellum. *Soft Matter* **12**:5613–5620. doi:10.1039/C6SM00526H

Li B, Cao Y-P, Feng X-Q, Gao H. 2012. Mechanics of morphological instabilities and surface wrinkling in soft materials: a review. *Soft Matter* **8**:5728–5745. doi:10.1039/C2SM00011C

Liang H, Mahadevan L. 2011. Growth, geometry, and mechanics of a blooming lily. *Proc Natl Acad Sci USA* **108**:5516–5521. doi:10.1073/pnas.1007808108

Liang H, Mahadevan L. 2009. The shape of a long leaf. *Proc Natl Acad Sci USA* **106**:22049–22054. doi:10.1073/pnas.0911954106

Madsen JS, Lin Y-C, Squyres GR, Price-Whelan A, de Santiago Torio A, Song A, Cornell WC, Sørensen SJ, Xavier JB, Dietrich LE. 2015. Facultative control of matrix production optimizes competitive fitness in *Pseudomonas aeruginosa* PA14 biofilm models. *Appl Environ Microbiol* **81**:8414–8426. doi:10.1128/AEM.02628-15

Meylan S, Andrews IW, Collins JJ. 2018. Targeting antibiotic tolerance, pathogen by pathogen. *Cell* **172**:1228–1238. doi:10.1016/j.cell.2018.01.037

Nayar VT, Weiland JD, Nelson CS, Hodge AM. 2012. Elastic and viscoelastic characterization of agar. *J Mech Behav Biomed Mater* **7**:60–68. doi:10.1016/j.jmbbm.2011.05.027

Nerenberg R. 2016. The membrane-biofilm reactor (MBfR) as a counter-diffusional biofilm process. *Curr Opin Biotechnol* **38**:131–136. doi:10.1016/j.copbio.2016.01.015

Ogden RW. 1997. Non-linear Elastic Deformations. Mineola: Dover Publications. ISBN:978-0-486-69648-5

Okegbe C, Price-Whelan A, Dietrich LE. 2014. Redox-driven regulation of microbial community morphogenesis. *Curr Opin Microbiol* **18**:39–45. doi:10.1016/j.mib.2014.01.006

O'Toole G, Kaplan HB, Kolter R. 2000. Biofilm formation as microbial development. *Annu Rev Microbiol* **54**:49–79. doi:10.1146/annurev.micro.54.1.49

Persat A, Nadell CD, Kim MK, Ingremeau F, Siryaporn A, Drescher K, Wingreen NS, Bassler BL, Gitai Z, Stone HA. 2015. The mechanical world of bacteria. *Cell* **161**:988–997. doi:10.1016/j.cell.2015.05.005

Peterson BW, He Y, Ren Y, Zerdoum A, Libera MR, Sharma PK, van Winkelhoff A-J, Neut D, Stoodley P, van der Mei HC, Busscher HJ. 2015. Viscoelasticity of biofilms and their recalcitrance to mechanical and chemical challenges. *FEMS Microbiol Rev* **39**:234–245. doi:10.1093/femsre/fuu008

Qi Y, Kim J, Nguyen TD, Lisko B, Purohit PK, McAlpine MC. 2011. Enhanced piezoelectricity and stretchability in energy harvesting devices fabricated from buckled PZT ribbons. *Nano Lett* **11**:1331–1336. doi:10.1021/nl104412b

Rodriguez EK, Hoger A, McCulloch AD. 1994. Stress-dependent finite growth in soft elastic tissues. *J Biomech* **27**:455–467. doi:10.1016/0021-9290(94)90021-3

Shyer AE, Tallinen T, Nerurkar NL, Wei Z, Gil ES, Kaplan DL, Tabin CJ, Mahadevan L. 2013. Villification: How the gut gets its villi. *Science* **342**:212–218. doi:10.1126/science.1238842

Skorupski K, Taylor RK. 1996. Positive selection vectors for allelic exchange. *Gene* **169**:47–52. doi:10.1016/0378-1119(95)00793-8

Solon J, Kaya-Çopur A, Colombelli J, Brunner D. 2009. Pulsed forces timed by a ratchet-like mechanism drive directed tissue movement during dorsal closure. *Cell* **137**:1331–1342. doi:10.1016/j.cell.2009.03.050

Tallinen T, Chung JY, Rousseau F, Girard N, Lefèvre J, Mahadevan L. 2016. On the growth and form of cortical convolutions. *Nat Phys* **12**:588–593. doi:10.1038/nphys3632

Thompson DW. 1992. On Growth and Form. Cambridge: Cambridge University Press. ISBN:978-0-521-43776-9

Thongsomboon W, Serra DO, Possling A, Hadjineophytou C, Hengge R, Cegelski L. 2018. Phosphoethanolamine cellulose: A naturally produced chemically modified cellulose. *Science* **359**:334–338. doi:10.1126/science.aao4096

Vella D, Bico J, Boudaoud A, Roman B, Reis PM. 2009. The macroscopic delamination of thin films from elastic substrates. *Proc Natl Acad Sci USA* **106**:10901–10906. doi:10.1073/pnas.0902160106

Wang Q, Zhao X. 2015. A three-dimensional phase diagram of growth-induced surface instabilities. *Sci Rep* **5**:8887. doi:10.1038/srep08887

Wilking JN, Zaburdaev V, De Volder M, Losick R, Brenner MP, Weitz DA. 2013. Liquid transport facilitated by channels in *Bacillus subtilis* biofilms. *Proc Natl Acad Sci USA* **110**:848–852. doi:10.1073/pnas.1216376110

Yamada KM, Cukierman E. 2007. Modeling tissue morphogenesis and cancer in 3D. *Cell* **130**:601–610. doi:10.1016/j.cell.2007.08.006

Yan J, Moreau A, Khodaparast S, Perazzo A, Feng J, Fei C, Mao S, Mukherjee S, Košmrlj A, Wingreen NS, Bassler BL, Stone HA. 2018. Bacterial biofilm material properties enable removal and transfer by capillary peeling. *Advanced Materials* **30**:1804153. doi:10.1002/adma.201804153

Yan J, Nadell CD, Stone HA, Wingreen NS, Bassler BL. 2017. Extracellular-matrix-mediated osmotic pressure drives *Vibrio cholerae* biofilm expansion and cheater exclusion. *Nat Commun* **8**:327. doi:10.1038/s41467-017-00401-1

Zhang C, Li B, Huang X, Ni Y, Feng X-Q. 2016. Morphomechanics of bacterial biofilms undergoing anisotropic differential growth. *Appl Phys Lett* **109**:143701. doi:10.1063/1.4963780

Zhang C, Li B, Tang J-Y, Wang X-L, Qin Z, Feng X-Q. 2017. Experimental and theoretical studies on the morphogenesis of bacterial biofilms. *Soft Matter* **13**:7389–7397. doi:10.1039/C7SM01593C

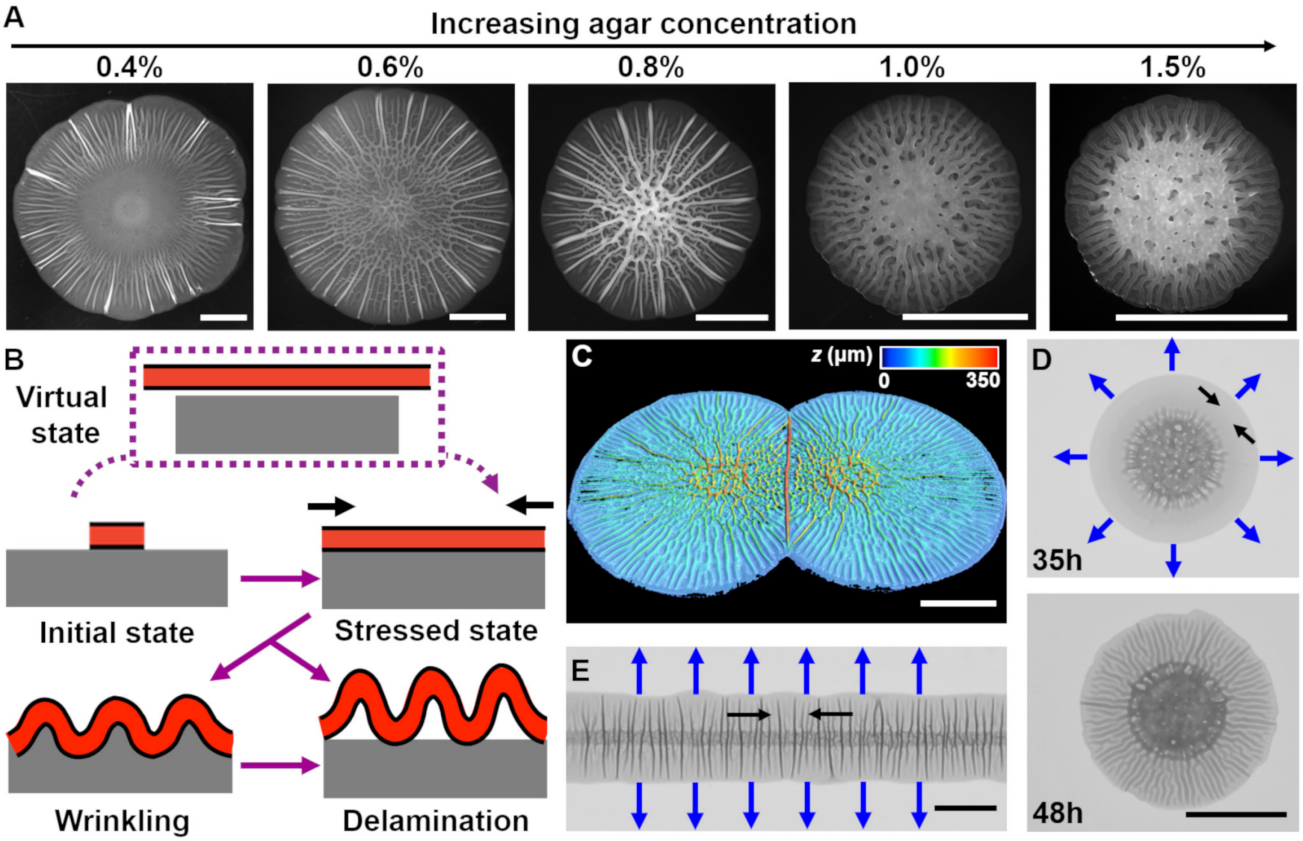

Figure 1. Mechanical instability drives *V. cholerae* biofilm morphogenesis. (A) Bright-field images of biofilms grown for 2 days on the designated percentages of agar. (B) Schematic of the wrinkling and delamination processes during biofilm expansion. Red with black outline denotes the biofilm. Gray denotes the substrate, agar in this case. See text for details. (C) Three-dimensional (3D) profile of two colliding biofilms, initially inoculated 9 mm apart, grown on a 0.6% agar plate for 36 h. (D) Transmission image of a *V. cholerae* biofilm grown for 35 h (*top*) and 48 h (*bottom*) on a 1.0% agar plate. (E) Transmission image of a *V. cholerae* biofilm inoculated as a line and grown for 30 h on a 0.5% agar plate. In D and E, blue arrows denote the expansion directions, and black arrows denote the tangential directions along which compressive stress accumulates. All scale bars are 5 mm.

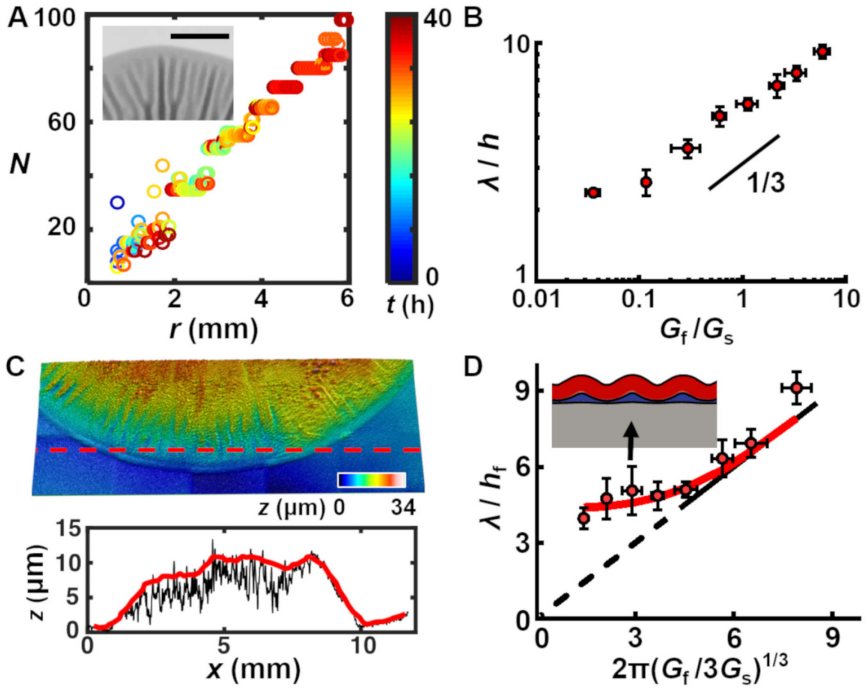

Figure 2. A trilayer mechanical model predicts the intrinsic wavelength of the biofilm pattern. (A) Number of wrinkles/blisters N versus radial coordinate r during biofilm growth. The color scale indicates growth time t. Inset: Closeup transmission image of a growing biofilm shows that wrinkles/blisters bifurcate to maintain a constant λ. Agar concentration: 0.7%, scale bar: 2 mm. (B) The scaling relationship between λ (normalized by the biofilm thickness h) and the shear modulus ratio G_f/G_s between the biofilm and the agar substrate. The black line indicates a slope of 1/3 on a log-log scale. (C) Characterization of the debris layer. *Top*: 3D topography of the remaining debris layer after peeling a biofilm off an agar substrate. *Bottom*: height profile extracted along the contour indicated by the dashed red line in the *top* panel. Both the raw (black) and smoothed (red) data are shown, from which the debris layer thickness h_d was calculated. (D) Replot of the data in B taking into account the debris layer. The corrected biofilm thickness h_f was obtained by subtracting the debris thickness h_d from the total thickness h. The black dotted line corresponds to a line of slope of 1 extending to the origin. The solid portion of the black line

corresponds to the prediction from the bilayer model, which applies only to x coordinates greater than 4.75 (Wang and Zhao, 2015). The red line is the fitted data from the trilayer model in which the stiffness contrast between the debris and biofilm layers G_d/G_f is treated as a fitting parameter while holding h_d/h_f = 0.3. Inset: finite-element simulation of the trilayer model undergoing wrinkling instability. Red denotes the biofilm. Gray denotes the substrate. Blue denotes the debris layer. Simulation parameters were chosen to mimic the growth condition on 1.0% agar (black arrow). Data are represented as mean ± std with n = 3.

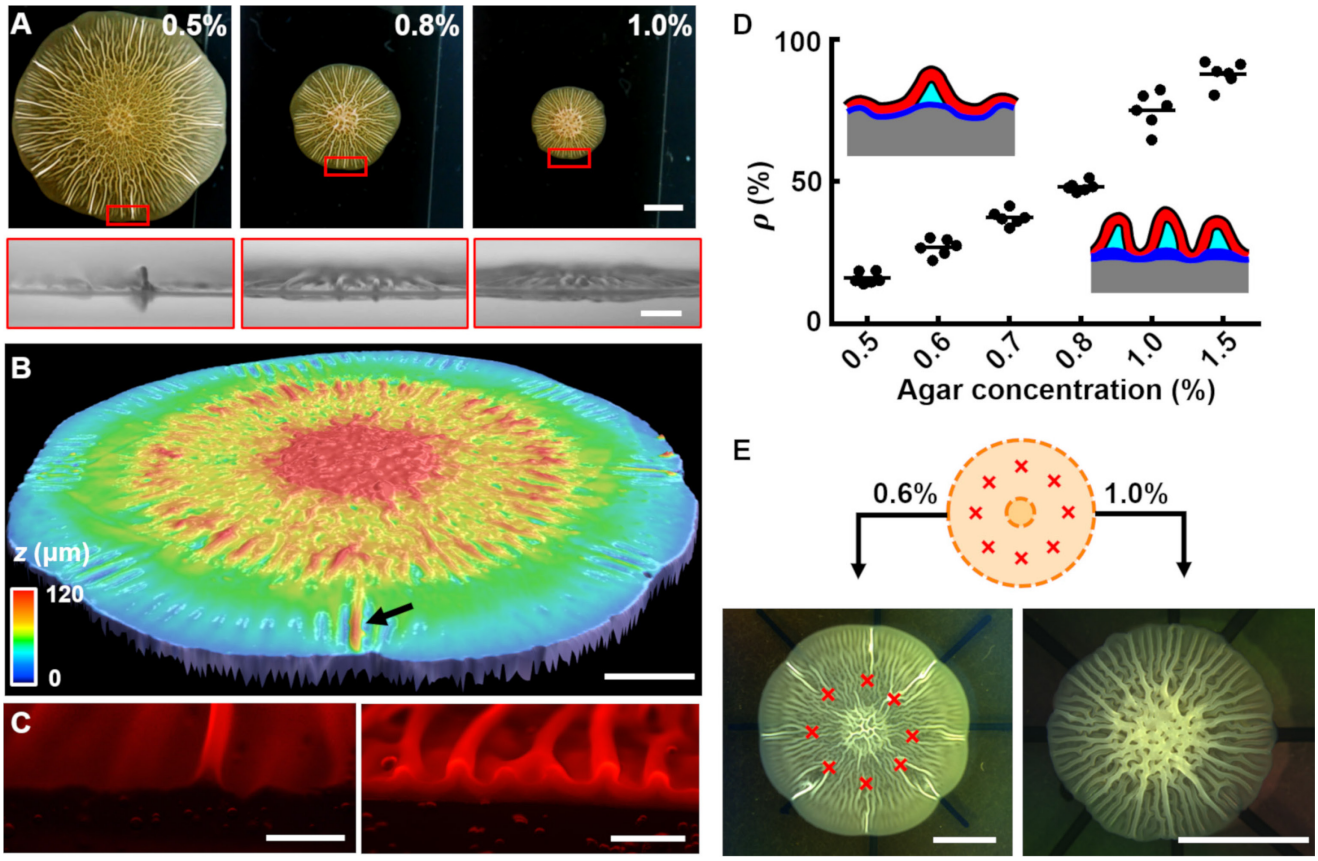

Figure 3. The biofilm wrinkling-to-delamination transition is controlled by adhesion energy. (A) Top (*top*) and side (*bottom*) views of biofilms on plates containing the designated concentrations of agar taken 10 h after the onset of delamination. Scale bar: 5 mm (*top*) and 1 mm (*bottom*). (B) Surface topography of a biofilm grown on 0.5% agar at the onset of the wrinkling-to-delamination transition (36 h). Arrow indicates a blister. Scale bar: 2 mm. (C) Cross-sectional views of rims of biofilms producing fluorescent mKate2, grown for 40 h on plates containing 0.6% agar (*left*) and 1.0% agar (*right*). Scale bars: 0.5 mm. (D) Percentage (ρ) of blisters in all radially oriented features (wrinkles + blisters) versus agar substrate concentration for 2-day-old biofilms. Insets: schematics showing how ρ depends on substrate stiffness. Red with black outline, biofilms; gray, agar substrate; blue, debris layer; cyan, liquid between the blisters and the agar. (E) Biofilm growth on a substrate with defined defects. *Top*: schematic. Yellow denotes the growing biofilm. Red crosses

denote the eight defects generated by manually making holes in the agar. *Bottom*: bright-field
595 images of typical experiments using the setup shown on the *Top*, for biofilms grown on plates with the designated agar concentrations. Scale bars: 5 mm.

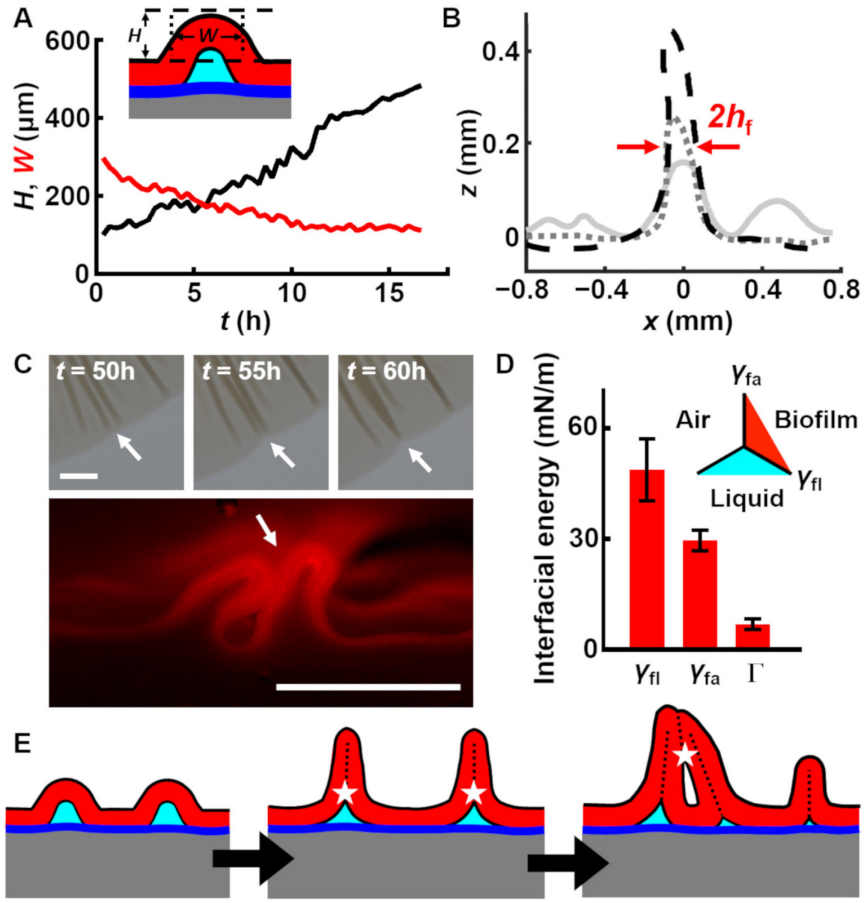

Figure 4. Interfacial energies control blister dynamics and interactions between blisters. (A) Time evolution of height H (black) and width W (red) of a representative biofilm blister. Inset: schematic representation of a blister; color code as in Figure 3D. (B) Developing profile of a single blister, extracted from side view images at successive time points after delamination. Profiles are shown at 2.5 h (gray line), 10 h (gray dotted line) and 17.5 h (black dashed line) after the onset of delamination. The distance between the red arrows corresponds to W, which, over time, approaches twice the biofilm thickness ($2h_f$). Agar concentration: 0.4%. (C) Representative merging of adjacent blisters (white arrows) at specified times (*top*). Cross section image from a biofilm producing fluorescent mKate2 reveals blister peak-to-peak contact (*bottom*; designated by the white arrow). Agar concentration: 0.7%. Scale bars: 1 mm (*top*) and 0.5 mm (*bottom*). (D) Interfacial energy of the biofilm-air interface γ_{fa}, biofilm-liquid interface γ_{fl}, and the adhesion

energy between the biofilm and the substrate Γ for WT *V. cholerae* biofilms. Data are represented as mean ± std with $n = 3$. *Inset*: schematic of different interfaces. (E) Schematic of blister development in a WT *V. cholerae* biofilm. White stars and dashed black lines denote interface annihilation events. For D and E, color code as in Figure 3D.

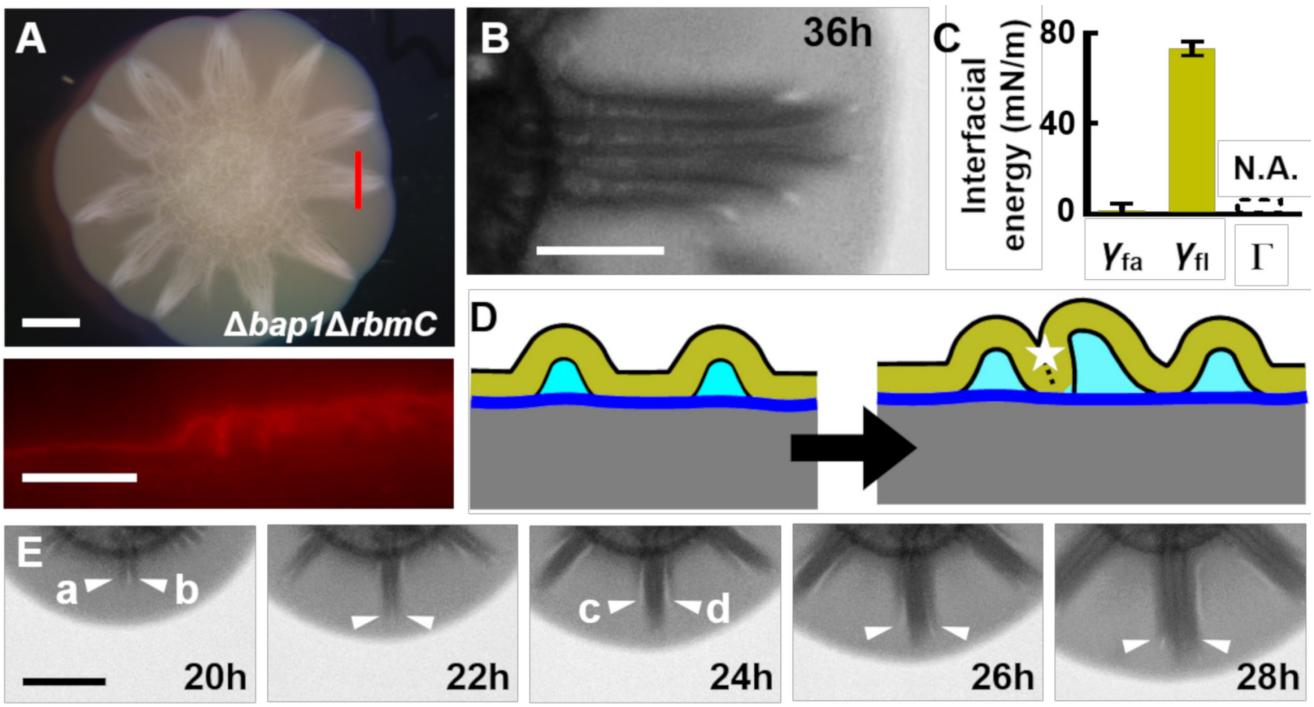

Figure 5. Morphogenesis of a mutant biofilm possessing altered interfacial energies. (A) Bright-field (*top*) and cross-sectional (*bottom*) images of a *V. cholerae* Δ*bap1*Δ*rbmC* (abbreviated as Δ*BC* below) mutant biofilm producing fluorescent mKate2, grown for 2 days on a 0.6% agar substrate. The red line in the *top* panel indicates the location of the cross section used for the *bottom* panel. Scale bars: 2 mm (*top*) and 500 μm (*bottom*). (B) Closeup view of a star facet in a Δ*BC* biofilm grown on 0.6% agar for 36 h. Scale bar: 1 mm. (C) Interfacial energies measured for the Δ*BC* biofilm. N.A. means too small to be measured. Data are represented as mean ± std with $n = 3$. (D) Schematic representations of Δ*BC* biofilm morphology development. Color code as in Figure 3D, except that yellow represents the Δ*BC* biofilm. (E) Transmission images of a section of a Δ*BC* biofilm growing on a 0.6% agar plate at the designated times. White arrowheads indicate emerging blisters. Four blisters (a-d) emerged during the time shown. Scale bar: 1 mm.

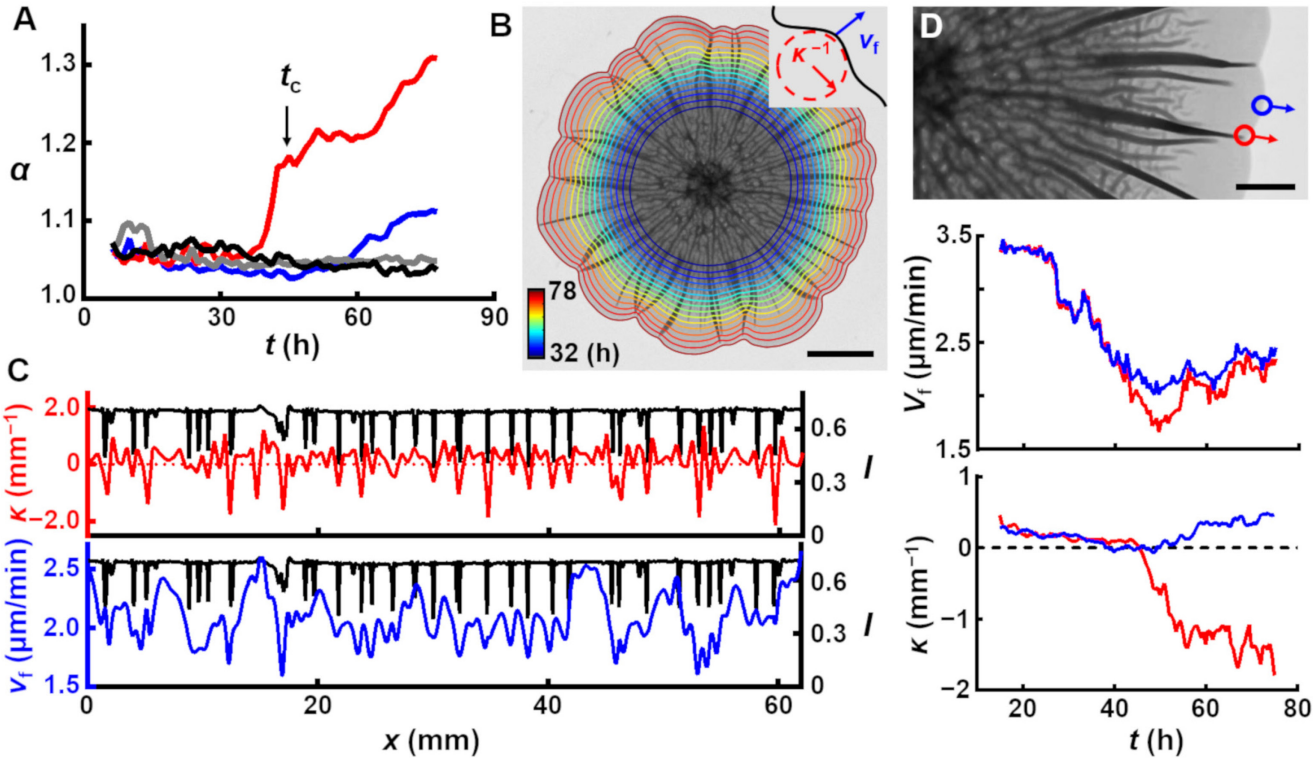

630 Figure 6. Delamination defines the overall biofilm contour. (A) Time evolution of asphericity index α (see text for definition) of the biofilm contour. Two agar substrate concentrations are shown (0.4%, red; 1.0%, blue) for WT *V. cholerae* biofilms. The sharp upturn in α defines the critical time t_c. Biofilms lacking matrix (Δ*vpsL* mutant; 0.4%, gray) or possessing an unstructured matrix (Δ*rbmA*Δ*bap1*Δ*rbmC* mutant; 0.4%, black) remain circular. (B) Image of a WT *V. cholerae* 635 biofilm grown on 0.7% agar 78 h after inoculation, overlaid with the time evolution of the biofilm boundary. Colors correspond to the expanding boundary from 32 to 78 h. Scale bar: 5 mm. *Inset*: schematic of local velocity V_f and the inverse of local curvature κ^{-1}. (C) Transmitted light intensity profiles I (black), κ (red), and V_f (blue) along the biofilm periphery from panel B at 60 h. (D) *Top*: partial image of the same biofilm shown in B at 75 h. Red and blue dots denote two boundary 640 points at the locations of a delaminated and a flat region, respectively. Arrows indicate boundary

expansion. *Middle* and *Bottom*: time evolution of V_f and κ of the designated points during biofilm development, respectively. Scale bar: 2 mm.

Material and Methods

Key Resource table

REAGENT or RESOURCE	SOURCE	IDENTIFIER
Bacterial and Virus Strains		
V. cholerae vpvC^{W240R} Δ*pomA*	(Yan et al., 2017)	N/A
V. cholerae vpvC^{W240R} Δ*pomA lacZ*:P_{tac}-*mKate2*:*lacZ*	(Yan et al., 2017)	N/A
V. cholerae vpvC^{W240R} Δ*pomA*Δ*bap1*Δ*rbmC*	(Yan et al., 2017)	N/A
Chemicals, Peptides, and Recombinant Proteins		
LB broth, Miller	Fisher Scientific	Cat# BP1426-2
Bacto agar	VWR	Cat# 214030
O.C.T. agent	Tissue-Tek, Sakura	Cat# 4583
Silicone oil, 5 cSt	Sigma Aldrich	Cat# 317667
Software and Algorithms		
MATLAB and Image Processing Toolkit	Mathworks, 2015	https://www.mathworks.com/products/matlab.html
PRISM version 6.07	GraphPad, 2015	https://www.graphpad.com/scientific-software/prism/
Image composite editor version 2.0.3	Microsoft, 2015	https://www.microsoft.com/en-us/research/project/image-composite-editor/
Gmsh version 3.0.6	(Geuzaine and Remacle, 2009)	https://gmsh.info
Paraview version 5.5.0	(Ahrens et al., 2005)	https://www.paraview.org/
FEniCS version 2017.2.0	(Alnæs et al., 2015)	https://fenicsproject.org/
DigiCamControl software version 2.0.72.0	DigiCamControl, 2015	http://digicamcontrol.com/
Leica Map Start version 7.4.8051	Leica, 2017	https://www.leica-microsystems.com/products/microscope-software/details/product/leica-map/
ImageJ and freehand line selection tool	NIH	https://imagej.nih.gov/ij/
RheoPlus version 3.40	Anton Paar, 2008	N/A
Other		
Physica MCR 301 shear rheometer	Anton Paar, 2008	N/A

Nikon D3300 SLR digital camera with DX Zoom-Nikkor 18-55 mm lens	Amazon	https://www.amazon.com/Nikon-1532-18-55mm-3-5-5-6G-Focus-S/dp/B00HQ4W1QE/ref=sr_1_3?ie=UTF8&qid=1492108083&sr=8-3&keywords=D3300&th=1
Huion L4S light box	Amazon	https://www.amazon.com/Huion-L4S-Light-Box-Illumination/dp/B00J0UUHPO
Sigma 105 mm macro lens for Nikon DSLR camera	Amazon	https://www.amazon.com/Sigma-258306-105mm-Macro-Camera/dp/B0058NYW3K/ref=sr_1_sc_3?ie=UTF8&qid=1485483491&sr=8-3-spell&keywords=sigma+macroles
Leica stereoscope model M205 FA	Leica	N/A
Leica DCM 3D micro-optical system	Leica	https://www.leica-microsystems.com/products/light-microscopes/upright-microscopes/details/product/leica-dcm-3d/
VR3200 wide-area 3D measurement system	Keyence	https://www.keyence.com/products/measure-sys/3d-measure/vr-3000/models/vr-3200/index.jsp

Experimental Model and Subject Details

Bacterial strains:

All *Vibrio cholerae* strains used in this study are derivatives of *V. cholerae* O1 biovar El Tor strain C6706, harboring a missense mutation in the *vpvC* gene (VpvC W240R) (Beyhan and Yildiz, 2007). Additional mutations were engineered into this strain using *Escherichia coli* S17 λ*pir* and the pKAS32 vector (Skorupski and Taylor, 1996).

Bacterial growth:

Bacterial cultures were grown at 37°C under constant shaking in standard lysogeny broth (LB) medium. LB medium solidified with different percentages of agar was used as the solid support to grow biofilms.

Methods Details

Biofilm growth on agar plates:

V. cholerae strains were streaked onto LB plates containing 1.5% agar and grown at 37°C overnight. Individual colonies were selected and inoculated into 3 mL of LB liquid medium containing glass beads and the cultures were grown with shaking at 37°C to mid-exponential phase (5-6 h). Subsequently, the cultures were mixed by vortex, OD_{600} was measured, and the cultures were back diluted to an OD_{600} of 0.5. 1 μL of this preparation was spotted onto pre-warmed plates that had been solidified with different percentages of agar. Subsequently, the plates were incubated at 37°C. Typically, four colonies were grown per agar plate. For time-lapse imaging, one or two colonies were grown on each plate.

Bright field imaging:

Biofilms were imaged with a Leica stereoscope in the reflective (bright field) mode. For biofilms larger than the field view, multiple overlapping images were acquired manually (3 by 3 or 3 by 2) at different locations in the biofilm.

3D optical profiling:

Biofilms were imaged with a Keyence VR-3200 optical profiler using a telecentric multi-triangulation algorithm.

Transmission imaging:

A custom transmission imaging setup was built in a 37°C environmental room to follow biofilm growth. Briefly, an agar plate containing the inoculum was placed on an LED illumination pad (Huion L4S Light Box) and imaged with a Nikon D3300 SLR camera equipped with a Sigma 105 mm F2.8 Macro Lens. The entire setup was covered with a dark board. The camera was controlled using DigiCamControl software. Imaging was started 5 h after inoculation at which time the camera was capable of focusing on the growing biofilm. Imaging was performed automatically every 15 min for 3 days.

Side-imaging:

A similar setup to the one described in the preceding paragraph was used to image biofilms from the side, with the following changes. First, the LED illumination pad was placed on the side so that the camera received scattered light from the biofilm surface. Second, an additional camera (Nikon D3300 SLR equipped with DX Zoom-Nikkor 18-55 mm lens) was also placed on the side of the biofilm, close to 90° with respect to the first optical path. To remove the optical obstruction from the wall of the agar plate, an imaging window (~ 1 cm × 1 cm) was created using a hot razor blade. Imaging started immediately before the onset of the wrinkling-to-delamination transition, and the time interval between images was 5 min. From time to time, the focus in the side view was adjusted manually.

Cross-sectioning of biofilms:

Biofilms of *V. cholerae* strains expressing *mKate2* were grown on agar plates as described above. The region of the agar substrate containing a biofilm (~ 2.5 cm × 2.5 cm) was removed and transferred to an empty petri dish. O.C.T. agent (Tissue-Tek, Sakura) was applied to the surface of the biofilms, and the entire petri dish was rapidly dipped into a dry ice-ethanol mixture to solidify the O.C.T. agent together with the biofilm. Razor blades were used to cut through the solidified samples. Samples with exposed cross-sections were immediately transferred to a homemade T-shaped sample holder and kept frozen in a dry ice-ethanol mixture. These samples were transferred to a Leica stereoscope and imaged in bright field mode or in fluorescent mode with an mCherry filter set.

Biofilm growth on substrates with defined defects:

On prewarmed agar plates, syringe needles were used to punch holes at eight locations, equally spaced by 45°, along a circle that would encompass the biofilm. The diameter of the circle was ~ 1 cm for biofilms grown on 0.6% agar and ~ 0.4 mm for biofilms grown on 1.0% agar. The inoculant was spotted at the center of the circle.

Biofilm growth in a line geometry:

A *V. cholerae* culture at OD_{600} = 0.5 was prepared as described above. A sterile razor blade was carefully dipped into this culture and dried in air for 1 min. The razor blade was gently touched to the surface of a prewarmed agar plate to initiate biofilm growth.

Biofilm growth at the liquid-air interface:

First, a biofilm was grown for 24 h following the procedure describe above. Subsequently, 25 mL of LB medium was gently added from the edge of the agar plate. When the liquid reached the biofilm, the liquid lifted the biofilm off the substrate by capillary force. The subsequent growth of the biofilm floating at the air-liquid was monitored using the homemade imaging setup described above with images acquired at 5 min intervals.

Rheological measurements of biofilm properties:

All rheological measurements were performed with a stress-controlled shear rheometer (Anton Paar Physica MCR 301) at 37°C. For each measurement, 100-960 colonies were collected with a pipette tip or a razor blade and transferred onto the lower plate of the rheometer. After sandwiching the biofilm cells between the upper and lower plates with a gap size of 0.5 mm, silicone oil (5 cSt at 25°C, Sigma Aldrich) was applied to surround the biofilm. Sandblasted surfaces were used for both the upper and lower plates to avoid slippage at the boundary. Oscillatory shear tests were performed with increasing amplitudes of the oscillatory strain ε' from 0.01 – 2000% at a fixed frequency of 6.28 rad/s. The storage modulus G' was extracted with the RheoPlus software as a function of ε'. The Poisson ratio ν of the biofilm was estimated to be ~ 0.49, by compressing the biofilm in the vertical direction and measuring its bulk modulus. The modulus of the biofilm was measured and remained roughly constant for the first 48 h.

Rheological measurement of agar:

LB medium containing different agar concentrations was freshly prepared in 100 mL bottles. The semi-solid medium was heated in a microwave, cooled to ~ 55°C, and added (2 mL) to the lower plate of the rheometer preheated to 60°C. The heated agar solution was subsequently sandwiched

between the two rheometer plates with a gap size of 5 mm and sealed with silicone oil. The preparation was cooled to 22°C using a cooling rate of 1°/min. Subsequently, the solid agar was heated to 37°C for measurement. This procedure mimics the sequence of events that agar plates underwent in our hands during preparation and biofilm growth. Smooth surfaces with TrueGap technology were used. Oscillatory shear tests were performed in the linear elastic region at a fixed frequency of 6.28 rad/s.

Biofilm thickness measurements:

The surface profiles of biofilms grown for 48 h were analyzed with a Leica DCM 3D Micro-optical System. A 10× objective was used to image a 3 by 3 region covering roughly one quarter of the biofilm, with a *z* step size of 2 μm. To measure the thickness of the debris layer, agar plates containing biofilms were slowly vertically lowered into water to peel the biofilms from the substrate. After drying, the above analysis procedure was performed to measure the thickness of the remaining debris layers.

Quantification and Statistical Analysis

Statistics

Error bars correspond to standard deviations of the means. Standard *t*-tests were used to compare treatment groups and are indicated in each figure legend. Tests were always two-tailed and unpaired as demanded by the details of the experimental design. All statistical analyses were performed using GraphPad Prism software.

Biofilm thickness measurement

The total thickness of the biofilm h and the thickness of the debris layer h_d were measured using LeicaMap software analyses of the reflective confocal images. A three-point flattening procedure was first performed on the agar surface to level the image. Next, three line profiles were generated at different locations spanning the agar surface to the surface of the biofilm or the debris layer. An automatic step size detection procedure was performed with a built-in function in the software to extract h or h_d. The three measured values were averaged to give the value for one biological replicate. The biofilm thickness h_f was obtained by $h_f = h - h_d$.

Shear modulus analysis

For data obtained with biofilms, segmented linear fittings were applied to G'-ε' curves on a log-log scale. G' varies minimally in the plateau region. We used the fitted G' value at $\varepsilon' = 1\%$ as the modulus of the biofilm G_f. For data obtained with agar, we averaged 10-20 points in the plateau region of the $G'(\varepsilon')$ curve to give G_s.

Processing of bright field images

Images from multiple locations in biofilms were stitched together with the Image Composite Editor software from Microsoft to yield the full images of the biofilms while preserving the original resolution. Raw images from the stereoscope contain iridescence due to reflections from agar, which were removed by setting the color saturation to zero (i.e., converting to black-and-white images).

Analysis of the transmission images

Image analyses were performed with custom codes written in Matlab and with ImageJ software. Raw transmitted light image data were first converted into intensity images. From the pixel intensity distributions, we identified the peak with the highest intensity and used it as background. We set the minimum intensity $I_{min} = 0$ and the average background intensity $\langle I_b \rangle = 0.9$ to standardize the contrast of the images. Images were then smoothed with a median filter. The intensity images were further binarized (by thresholding) to separate the biofilm object F from the background. We used the image of each biofilm at $t = 12$ h following inoculation to define the center O_F for all time points. When mutations affecting biofilm morphology arose, they were manually excluded from the image analysis.

To extract the periodicity of the wrinkling/delamination pattern, we tracked their time evolution from images. For wavelength analysis, we applied fast Fourier transformation (FFT) to intensity functions $I^r(\theta)$ in a ring at time t and radial coordinate r, and identified $N(r,t)$ from the peak frequency in the power spectrum. We also verified the values by autocorrelation and manual counting. We plotted all data from different time points and fitted them with a linear function $N(r) = 2\pi r/\lambda$ to obtain the intrinsic wavelength λ. The radial coordinate at which N decreases to zero was defined as R_p. For images of biofilms grown in a line geometry, several values of N were extracted from multiple lines at different distances from the central line, averaged, and subsequently used to extract λ.

For contour analyses, we first obtained the biofilm object F from the binarized image. From the binarized object F, we extracted the perimeter P and area A of region F. At each time point, we calculated the asphericity α as $\alpha = P^2/4\pi A$. To define the radii for biofilms that were not strictly circular, we used $\langle R_f \rangle = \langle |\boldsymbol{r}_i - \boldsymbol{r}_O| \rangle_i$, averaged over all the points $\boldsymbol{r}_i$ on the circumference ∂F. $\langle R_f \rangle$ was then calculated over time to give $\langle R_f(t) \rangle$ versus t. Segmented linear regression with two

segments was used to quantify the expansion velocity of the biofilm $\langle V_f \rangle$ before and after the critical time t_c as a well as to define the critical time itself.

To capture local curvature κ and expansion velocity V_f, the smoothed boundary ∂F was locally approximated by quadratic polynomials $\boldsymbol{r}_{i,2}(t)$ at $\boldsymbol{r}_i$. The parametrized curve $x_{i,2}(t)$ and $y_{i,2}(t)$ allowed us to locally calculate the analytical curvature κ_i and normal $\boldsymbol{n}_i$ using the weighted central difference. Coarse-grained contours at time points t and $t+\Delta t$ were then connected by joining $\boldsymbol{r}_i(t)$ to its nearest neighbor $\boldsymbol{r}_i(t+\Delta t)$ in $\partial F_{t+\Delta t}$, yielding local velocities $V_{f,i} = |\boldsymbol{r}_i(t+\Delta t) - \boldsymbol{r}_i(t)|/\Delta t$.

Analyses of the side-views of blisters

Blister contours were manually extracted with ImageJ software and then smoothed. The baseline of the blister was obtained by averaging the z coordinate of the left and right bottom region of the blister. The blister height H was calculated as the distance between the peak of the blister to the baseline. The width of the blister W was measured at half of the blister height.

3D profiles of biofilms

All analyses related to obtaining the 3D profiles of biofilms were performed with the Keyence Analyzer software. Noise was first removed from the raw data to give smooth, continuous surface profiles. Surfaces corresponding to agar were excluded by setting upper and lower thresholds in height. 3D views of biofilms were rendered with a built-in function in the software. The corresponding line profiles were extracted along an arc centered at the center of the biofilm.

Theoretical Models and Data Fitting

Theoretical models

We adapted a trilayer model from previous work (Lejeune et al., 2016b), and modeled the biofilm system with the following three elastic components: the biofilm (top), the debris layer (middle), and the agar substrate (bottom) denoted with subscripts f, d, and s, respectively. Biofilm and debris layers were modeled as thin elastic sheets with thickness h_f and h_d, while the agar substrate was modeled as a thick elastic body with a thickness h_s, which is much larger than the thicknesses of the other two layers. The shear modulus and Poisson's ratio of the materials are denoted by G and ν, respectively. For theoretical calculations, we treated all elastic components as incompressible and hence, $\nu = 0.5$ (confirmed in the experimental measurements). In the simulation, the debris layer grows at the same rate as the biofilm layer, while the substrate does not grow. This growth difference induces a strain mismatch between the biofilm/debris layer and the substrate, ε.

Following previous studies (Lejeune et al., 2016a, p.), we applied the Föppl-von Kárman equation to the biofilm model. Assuming a sinusoidal profile of the surface undulations, we can write the longitudinal stress P in the film as:

$$P(n) = \frac{G_f h_f^2 n^2}{3} + \frac{K}{h_f n^2},$$

where n is the wavenumber and K is the combined stiffness of the debris layer and the substrate layer:

$$K = \frac{4G_s n}{n h_d (G_s/G_d - 1) + 2},$$

and by setting $G_s = G_d$, we could recover the classic result of $K = 2nG_s$ for the semi-infinite substrate. By numerically solving the nonlinear equation $dP/dn = 0$, we determined the minimal critical value of P for mechanical instability and the corresponding n gives the critical wavenumber n_{cr}. The wavelength at the onset of wrinkling was then calculated as $\lambda_{cr} = 2\pi/n_{cr}$. The critical stress

and strain were obtained by $P_{cr} = P(n_{cr})$ and $\varepsilon_{cr} = P_{cr}/3G_f$, respectively. Theoretical predictions from the bilayer model can simply be calculated by setting $G_s = G_d$.

The above model, despite assuming only small strains, accurately predicted the wavelength and critical stress/strain for finite strains (Lejeune et al., 2016a). We verified that the analytical predictions were in reasonable agreement with results obtained from finite element simulations.

Data fitting

The only unknown parameter in the model is the shear modulus of the debris layer G_d, which is difficult to probe experimentally. Therefore, we treated G_d as the only fitting parameter. We used $h_d/h_f = 0.3$ as an average value from the relevant experimental data and fit the model against the experimental data for wavelength versus stiffness contrast between the biofilm and the agar substrate. Fitting was carried out by minimizing the least-square error between the theoretically predicted and the experimentally measured wavelengths. A bisection method was employed that converged in fewer than 10 iterations.

Computational models

A plane-strain computational model was developed to take into account growth, large deformations, and nonlinear elasticity of the system. We considered the same planar three-layer structure as above. According to finite strain theory, we define the deformation gradient tensor as $F_{ij} = \partial x_i / \partial X_j$, where x_i and X_i denote the coordinates in the deformed and undeformed configuration, respectively (Ogden, 1997). To incorporate the effect of growth, we further introduced the decomposition of the deformation tensor $\boldsymbol{F} = \boldsymbol{F}_e\boldsymbol{F}_g$ as the product of the growth deformation $\boldsymbol{F}_g$ and the elastic deformation $\boldsymbol{F}_e$ (Figure S3) (Rodriguez et al., 1994). We used $\boldsymbol{F}_g =$

$\begin{pmatrix} 1+g & 0 \\ 0 & 1 \end{pmatrix}$ for the biofilm and debris layers to describe their 1D growth ($g > 0$) in the X_1 direction, and set $\boldsymbol{F}_g$ to be the identity matrix $\boldsymbol{I}$ for the non-growing agar substrate. The growth-induced compressive strain is thus $\varepsilon = g/(1+g)$. To account for the nonlinear stress-strain behavior of materials undergoing large deformations, all three layers were modeled as neo-Hookean materials. The strain energy density of each layer is given by (Ogden, 1997)

$$\Psi(\boldsymbol{F}_e) = \frac{\mu_e}{2}(I_C - 2 - 2\ln J) + \frac{\lambda_e}{2}(\ln J)^2,$$

where μ_e and λ_e are the Lamé parameters, and they are related to the shear modulus G and Poisson's ratio v

$$\mu_e = G, \qquad \lambda_e = \frac{2Gv}{1-2v}.$$

$I_C = \mathrm{tr}(\boldsymbol{F}_e^T \boldsymbol{F}_e)$ is the first invariant of the right Cauchy-Green deformation tensor $\boldsymbol{C} = \boldsymbol{F}_e^T \boldsymbol{F}_e$, and $J = \det(\boldsymbol{F}_e)$. The total elastic energy of the system can thus be calculated by

$$\Pi = \int_{\Omega_f} \Psi(\boldsymbol{F}_{e,f}) J_{g,f} d\boldsymbol{X} + \int_{\Omega_d} \Psi(\boldsymbol{F}_{e,d}) J_{g,d} d\boldsymbol{X} + \int_{\Omega_s} \Psi(\boldsymbol{F}_{e,s}) J_{g,s} d\boldsymbol{X},$$

where $\Omega_{f/d/s}$ denotes the volume occupied by biofilm/debris/substrate in the initial undeformed reference configuration, and $J_g = \det(\boldsymbol{F}_g)$ specifies the volume element change following growth. We assumed that the present instability pattern always seeks the lowest potential energy among all possible configurations at any time during biofilm growth, neglecting the viscoelasticity and plasticity of the biomaterials that could potentially lead to hysteresis in mechanical instability.

Finite element simulations

For the computational model, we considered a rectangular domain $\Omega = \Omega_f \cup \Omega_d \cup \Omega_s = [0, L] \times [0, h_f + h_d + h_s]$ composed of three layers, where L denotes the size of the system. We use subscripts 1

and 2 to denote the horizontal and vertical components, respectively. Numerically, the task is to calculate the displacement field $u_i = x_i - X_i$ that minimizes the total potential energy, i.e. $\boldsymbol{u} = \arg\min_{\boldsymbol{u}\in V_{\boldsymbol{u}}} \Pi$, where $V_{\boldsymbol{u}}$ is the function space that satisfies the boundary conditions on $\boldsymbol{u}$. Without loss of generality, we considered a scenario in which the biofilm and debris layers grow together but are confined by the left and right walls of the bottom fixed domain Ω, i.e., the boundary conditions were set by $u_1|_{X_1=0} = u_1|_{X_1=L} = u_2|_{X_2=0} = 0$ (Figure S3). The nonlinear constrained minimization problem was implemented in the open-source computing platform FEniCS (Alnæs et al., 2015). The computational model was discretized by first-order triangular elements generated by Gmsh (Geuzaine and Remacle, 2009), and the accuracy of the results were verified by mesh refinements. A growth increment of $\Delta g = 0.002$ was employed in the simulations, up to a maximum of 1. For each step, we computed the equilibrium configuration $\boldsymbol{x}$ and the Green-Lagrange strain tensor $\boldsymbol{e} = 0.5(\boldsymbol{F}_e^{\mathrm{T}}\boldsymbol{F}_e - \boldsymbol{I})$ of the system. The critical condition for wrinkling instability was identified as to be when the vertical displacement of the biofilm surpassed the threshold value ($0.01h_f$). We further calculated the deviatoric strain tensor $e'_{ij} = e_{ij} - 0.5\delta_{ij}e_{kk}$ and the von Mises equivalent strain $\varepsilon_{vM} = (2e'_{ij}e'_{ij}/3)^{1/2}$ (Jones, 2009) to visualize the strain distribution among the three layers. All results were visualized by software Paraview (Ahrens et al., 2005). For the model parameters, we set $h_d/h_f = 0.3$ based on the measured thickness values from experiments, and $h_s/h_f = 10$ to represent the thick substrate. The stiffness contrast $G_d/G_f = 0.1$ was used according to the optimal fitting value from theoretical curves, and we varied G_f/G_s from 0.02 to 10 to correspond to the experimental conditions. In all simulations, L was set to be larger than 10 times the wavelength to minimize the finite size effect, and the Poisson's ratios of all three layers were set to be 0.45 to ensure convergence of the algorithm.

Data and software availability

Data**:**

All raw experimental data that support the findings of this study are available from the corresponding authors upon request.

Software:

Custom-written Matlab scripts and simulation codes used in this study are available at https://github.com/f-chenyi/biofilm-morphogenesis.